Retinotopic Organization in Human Visual Cortex and the Spatial Precision of Functional MRI

Stephen A. Engel, Gary H. Glover and Brian A. Wandell

Department of Psychology, Neuroscience Program and Department of Diagnostic Radiology, Stanford University, Stanford, CA 94305, USA

A method of using functional magnetic resonance imaging (fMRI) to measure retinotopic organization within human cortex is described. The method is based on a visual stimulus that creates a traveling wave of neural activity within retinotopically organized visual areas. We measured the fMRI signal caused by this stimulus in visual cortex and represented the results on images of the flattened cortical sheet. We used the method to locate visual areas and to evaluate the spatial precision of fMRI. Specifically, we: (i) identified the borders between several retinotopically organized visual areas in the posterior occipital lobe; (ii) measured the function relating cortical position to visual field eccentricity within area V1; (iii) localized activity to within 1.1 mm of visual cortex; and (iv) estimated the spatial resolution of the fMRI signal and found that signal amplitude falls to 60% at a spatial frequency of 1 cycle per 9 mm of visual cortex. This spatial resolution is consistent with a linespread whose full width at half maximum spreads across 3.5 mm of visual cortex.

In a series of experiments, we measured the retinotopic organization of human cortical area V1 and identified the locations of other nearby retinotopically organized visual areas. We also used the retinotopic organization of human primary visual cortex to measure the spatial localization and spatial resolution that can be obtained from functional magnetic resonance imaging (fMRI) of human visual cortex.

Human primary visual cortex (area V1) is located in the occipital lobe within and surrounding the calcarine sulcus. Data from human lesion studies showed that neurons within area V1 are retinotopically organized, following a roughly polar coordinate system (Holmes, 1918, 1944; Horton and Hoyt, 1991a). As one moves from posterior to anterior in cortex, the representation of the visual field shifts from the center to the periphery. We will refer to this dimension of retinotopy as eccentricity. As one moves from the lower to the upper lip of the calcarine, the representation of the visual field shifts from the upper vertical meridian through the horizontal meridian to the lower vertical meridian. We will refer to this dimension of retinotopy as polar angle. The locations of several visual field landmarks are shown in Figure 1*A*, and the key features of the cortical anatomy are shown in Figure 1*B*.

Because of the retinotopic organization of visual areas, it is possible to create simple visual stimuli that generate continuous traveling waves of neural activity in visual cortex. The stimulus used to create the traveling wave and our initial measurements of the wave were described briefly in prior reports (Engel *et al.*, 1993, 1994). The travelling wave allows retinotopic organization to be measured more efficiently and with higher spatial precision than was possible in previous work that used static stimuli (Fox *et al.*, 1987; Schneider *et al.*, 1993; Shipp *et al.*, 1995; Tootell, *et al.*, 1995). As a result, our method has been used widely to measure retinotopic organization in V1 and adjacent cortical areas (DeYoe *et al.*, 1994, 1996; Sereno *et al.*, 1995, Worden *et al.*, 1995).

Here we present a new set of results using the traveling wave. First, from measurements of the motion of the traveling wave, we identified the borders between several retinotopically organized visual areas in the posterior occipital lobe. Second, we measured the function relating cortical position to visual field eccentricity within area V1. Third, from measurements of the reliability of the traveling wave we found that it is possible to localize activity to within 1.1 mm of visual cortex. Fourth, from measurements of the amplitude of the traveling wave using stimuli with various spatial frequencies, we estimated the spatial resolution of the fMRI signal. We found that signal amplitude falls to 60% of maximum at a spatial frequency of 1 cycle per 9 mm of visual cortex. This spatial resolution is consistent with a linespread whose full width at half maximum spreads across 3.5 mm of visual cortex.

Materials and Methods

Stimuli

Area V1 of human visual cortex responds well to patterned, flickering stimuli. Hence, to create a strong neural response within area V1 we used a contrast-reversing checkerboard. The mean luminance of the flickering checkerboard field was 92 cd/m^2; its contrast was close to 100%; its contrast reversal rate was 8 Hz. The checkerboard pattern was superimposed on a uniform field whose intensity was equal to the mean intensity of the checkerboard. The stimuli were projected onto a rear-projection viewing screen mounted within the scanner. Subjects were supine and viewed the display by means of a mirror placed above their eyes and housed in a custom-designed headpiece. Subjects' head positions were stabilized using a bite bar, and subjects were instructed to fixate the center of the display throughout the stimulus presentation period.

To create a traveling wave of neural activity within area V1, we changed the position of the checkerboard pattern slowly over time. Figure 2*A* shows an example of a stimulus designed to create a wave of activity traveling from posterior to anterior calcarine. The flickering rings moved slowly across the visual field. In our experiments we used both expanding ring and contracting ring stimuli. When an expanding ring stimulus reached the edge of the viewing aperture (12° radius), it was replaced by a new ring in the center of the display. When a contracting ring stimulus reached the center, it was replaced by a new ring at the edge of the stimulus aperture. In these experiments four cycles of this stimulus were presented at a rate of one cycle either every 32 or 48 s.

Figure 2*B* shows that as the ring moves, the stimulus at each point in the visual field alternates at 1/32 Hz; the stimulus at a location is a flickering contrast pattern half of the time and is the uniform gray background the other half of the time. This alternation is delayed for peripheral visual field locations compared with central ones.

The moving ring stimulus is designed to measure retinotopic organization with respect to visual eccentricity. The flickering checkerboard gives rise to sustained neural activity at each location that

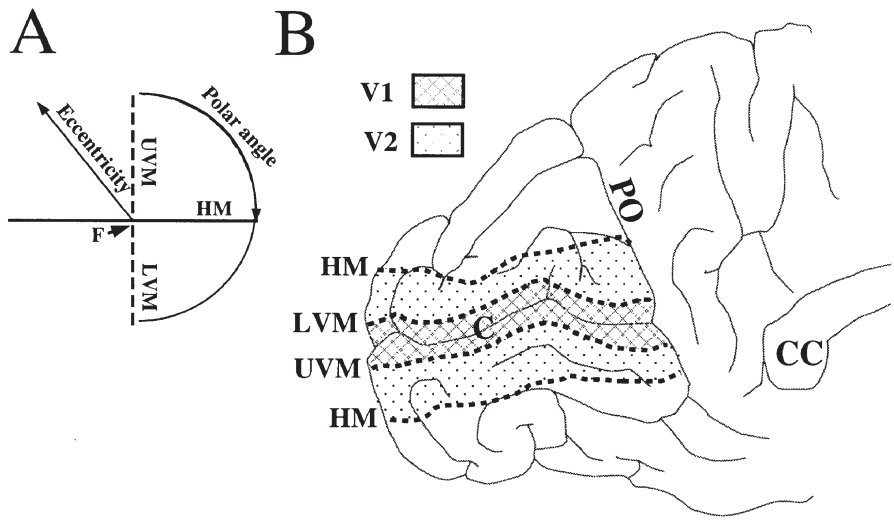

Figure 1. Visual field landmarks and their cortical representations are shown. (*A*) A representation of the visual field showing the fixation point (F), horizontal meridian (HM) and the upper and lower vertical meridia (UVM and LVM). The polar angle increases in the clockwise direction around the circle, and eccentricity increases from the fixation point to the peripheral visual field. (*B*) A medial view of human occipital lobe is shown. PO, Parieto-occipital sulcus; CC, corpus callosum; C, calcarine sulcus. The representations of the upper and lower vertical meridia are indicated by the dashed lines; these meridia define the borders between area V1 and the surrounding visual area, V2. An additional representation of the horizontal meridian runs along the deepest part of the calcarine sulcus and is not visible from this view point. Other representations of the horizontal meridian define the borders of dorsal V2 with area V3 and of ventral V2 with area VP. This figure was adapted from Horton and Hoyt (1991b).

modulates at the stimulus alternation frequency (1/32 Hz). As the stimulus moves from fovea to periphery the activity at locations containing neurons with peripheral receptive fields is delayed relative to locations containing neurons with foveal receptive fields, creating a traveling wave of neural activity. Because the neural activity alternates periodically, the delay can be measured by the phase of the neural activity.

To measure retinotopic organization with respect to polar angle, we used rotating patterns with three wedges, such as the one shown in Figure 2*C*, or a similar pattern with a single wedge. Subjects fixated at the center of the visual field while the wedges of contrast-reversing flicker, presented on a uniform gray field, rotated about the fixation point. The contrast reversal rate and the stimulus cycle time for the flickering wedges were the same as for the moving ring stimulus.

The rotating wedge stimulus is designed to measure retinotopic organization with respect to polar angle. As the stimulus rotates, activity at V1 locations containing neurons whose receptive fields are further along the direction of rotation will be delayed relative to locations containing neurons whose receptive fields are near the stimulus starting position. This stimulus creates a traveling wave of activity moving between the representations of the upper and lower vertical meridia. Again, because the neural activity alternates periodically, the delay can be measured by the phase of the neural activity.

Measurement Planes

Planes were selected in one of three orientations. To track activity traveling from posterior to anterior calcarine we acquired data in either a sagittal slice or an oblique plane parallel to the calcarine sulcus. To track activity traveling from the superior to the inferior lips of the calcarine we measured in a plane perpendicular to the calcarine sulcus.

Magnetic Resonance Protocols

Functional MR images were acquired continuously as subjects viewed the projected stimulus. Measurements were made with a GE Signa 1.5T scanner using a spiral k-space acquisition (Meyer *et al.*, 1992). We measured gradient-echo BOLD (T2*) contrast (Kwong *et al.*, 1992; Ogawa *et al.*, 1992).

In our initial experiments data were acquired in a single measurement plane using a typical TE of 40 ms, TR of 75 ms and flip angle of 23°. During each 192 s experiment, 128 images per plane were acquired (1.5 s/image) with an in-plane resolution of 1.03 mm and a through-plane resolution of 5 mm. The data were interpolated onto a 256 × 256 grid, yielding an in-plane pixel size of 0.78 mm.

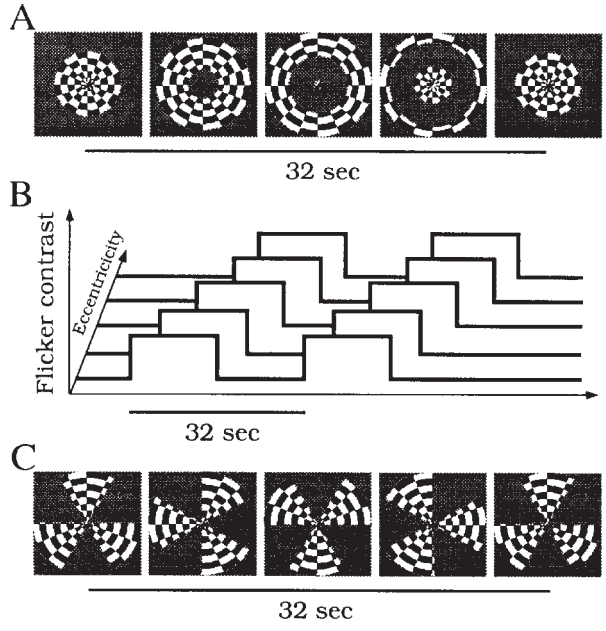

Figure 2. Stimuli used to create traveling waves of neural activity in retinotopically organized cortex are shown. The stimuli were composed of a contrast-reversing checkerboard pattern flickering at 8 Hz. (*A*) The expanding ring stimulus is shown at five moments in time spanning one stimulus cycle. (*B*) At each location within the visual field, the stimulus follows a square-wave alternation between the contrast-reversing rings and the uniform gray field. The expanding ring stimulus was delayed in the periphery relative to the center; hence, the temporal phase of the square-wave alternation varied as a function of distance from the center of the visual field. Two stimulus cycles are shown. (*C*) The rotating wedge stimulus is shown at five moments in time spanning one stimulus cycle.

In later experiments four or eight planes of data were acquired in each experiment; a typical TE was 40 ms, TR was 300 or 750 ms and flip angle was 35°. These experiments were of coarser spatial resolution: in-plane resolution was roughly 1.6 mm; through plane resolution was generally

4.0 mm. One image from each measurement plane was acquired every 2 s. In all experiments T1-weighted in-plane anatomical scans were taken in the functional measurement planes in order to register the functional and anatomical data. These anatomical images had an in-plane spatial resolution of 0.78 × 0.78 mm and a through-plane resolution of 5 mm.

Data Analysis

Time Series Analysis

The fMRI protocol yielded a time series of data at each pixel. We used two quantities to characterize each pixel's responses. First, we used the phase of the harmonic function (harmonic functions here refer to the set of functions comprising sinusoids at any phase and frequency) at the stimulus frequency that best correlated with the time series data (Bandettini *et al.*, 1993). This *response phase* measures the relative delay of stimulus driven activity at each pixel. We used the signal delay to infer the location of the receptive fields of the neurons whose activity gave rise to that pixel's time series data. We calculated the response phase using the discrete Fourier transform of the time series (see Appendix).

Second, we measured *response magnitude* as the correlation between the pixel time series and the best-correlated harmonic at the stimulus alternation frequency. We used the response magnitude to create the activity maps (Fig. 5) and to perform the spatial resolution analysis (Fig. 11). The correlation coefficient is the amplitude of the response at the stimulus frequency divided by the square root of the time series power; this quantity was calculated using the discrete Fourier transform of the time series (see Appendix).

For most of the stimuli we used, the harmonic frequency that best correlated with the response was equal to the stimulus frequency. As we describe below, this need not be the case; for some types of stimuli a significant response occurred at other frequencies (see Fig. 6). For the other experiments we describe, the principal response was at the stimulus frequency.

In the analyses reported below, we selected pixels in one of two ways. Some analyses were performed along linear regions of interest that were selected by hand from in-plane anatomical images. Others were performed on all pixels that were identified as containing gray matter; these were selected as the first step in the cortical flattening method described below.

Images of Flattened Cortex

In order to visualize data from many measurement planes, we created a single flattened representation of cortex. We performed this analysis using a procedure described more fully elsewhere (Wandell *et al.*, 1996). The method is similar to other computational methods that have been developed for flattening cortex (Schwartz, 1990; Dale and Sereno, 1993; Carman *et al.*, 1995; Drury *et al.*, 1996).

Briefly, we created flattened representations in four steps. First, we acquired a volume of anatomical images that spanned the part of cortex to be flattened. Second, a connected volume of gray matter was identified in the anatomical data, using a graphical software tool. Third, a fully automated algorithm assigned image positions to the sampled set of the identified gray matter pixels. The planar representation of the samples was computed using an iterative algorithm based on metric multi-dimensional scaling. Fourth, the planar positions of the remaining gray matter points were assigned by interpolation. (The software used to create these images has been archived and can be obtained from http://white.stanford.edu)

To view the fMRI measurements on the flattened representation, the user identified corresponding locations in the in-plane anatomies and the anatomical volume. The fMRI measurements were aligned with the anatomical volume by finding the best (least-squares) translation and rotation between the set of corresponding anatomical locations (Arun *et al.*, 1987). From this alignment, each gray matter location that falls in the functional planes was assigned a functional measurement. We generated images of activity by displaying each gray matter point's functional measurement at its location in the flattened representation. In images of functional activity on the flattened cortical representation, only gray matter points that fell within the functional scan planes are shown.

After the gray matter locations were placed within the flattened image, they did not fill the image plane continuously. To generate a continuous representation of the data, we interpolated: each image pixel in the flattened representation was assigned a weighted average of the neighboring pixels that contained data. The weights assigned to each neighbor were a Gaussian function of the distance to that neighbor.

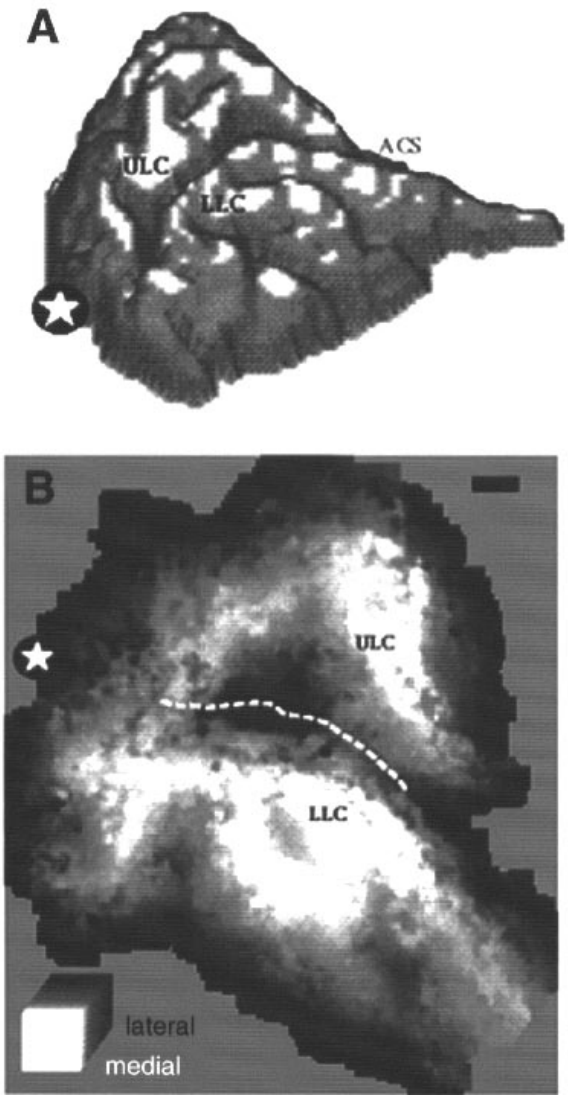

Figure 3. Two representations of the cortical sheet in the medial occipital lobe are shown. (*A*) A view of the medial surface of an occipital lobe is shown. ACS, anterior calcarine sulcus; ULC, upper lip of the calcarine; LLC, lower lip of the calcarine. The star represents a location near the occipital pole. (*B*) The same cortical region is shown in a flattened representation that was created by the method described in the text. The brightness of each image point represents the relative position along the medial–lateral axis in the brain. The dashed line traces the deepest part of the calcarine sulcus, and the star again indicates the location of the occipital pole. In this and all subsequent figures, scale bars indicate 1 cm.

Figure 3*A* is a view of the medial surface of an occipital lobe. Figure 3*B* is a flattened representation of this portion of cortex; the flattened representation was created using the algorithm described above. The position of each point in Figure 3*B* shows the location of a gray matter point in the flattened cortical manifold. The brightness of each point represents its relative position along the medial–lateral axis in the brain. Light points represent gray matter near the medial plane and dark points represent gray matter closer to the lateral aspect of the brain. The calcarine sulcus is easy to identify on the flattened representation

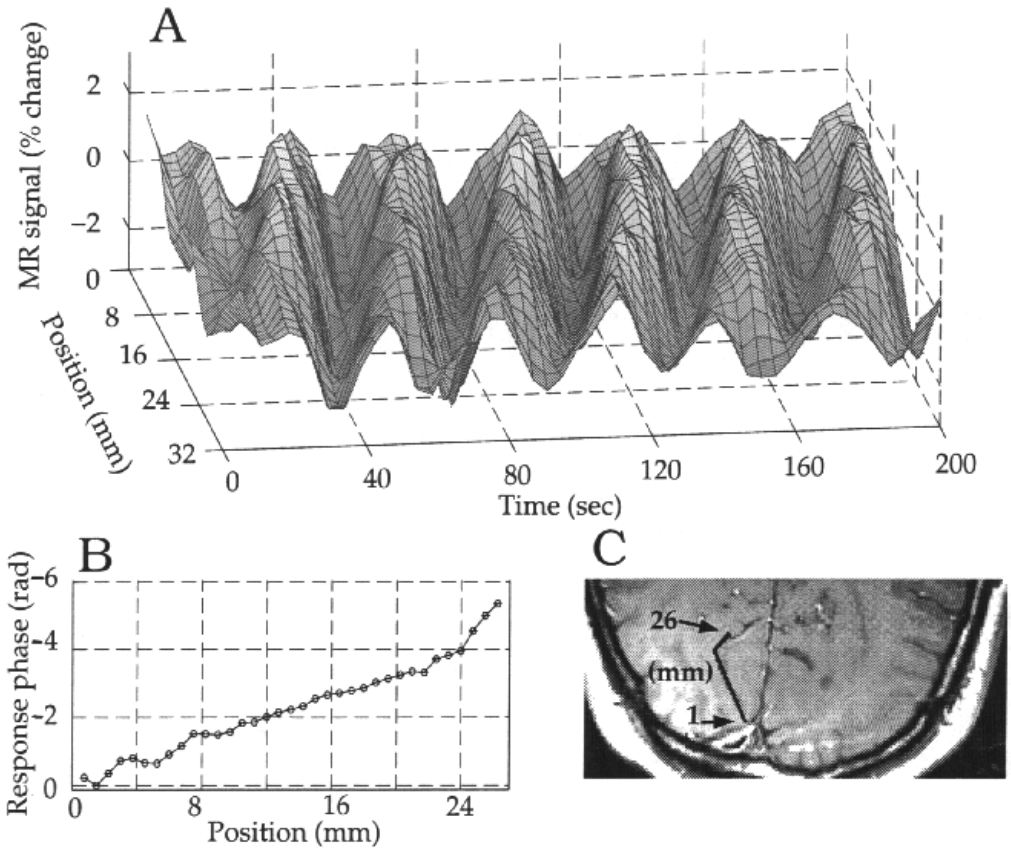

Figure 4. The traveling wave observed in area V1. (*A*) The time course of the fMRI signal at each of the locations within the region of interest during a single experiment is shown. The stimulus consisted of a single, contracting contrast-reversing ring, the stimulus period was 32 s and the stimulus was repeated six times. The horizontal axes show time and position along the region of interest. The vertical axis shows the deviation of the fMRI signal from the mean level. The plotted waveform is a smoothed version of the data, computed by convolving the fMRI data with a Gaussian kernel ($\sigma_x = 3$ mm, $\sigma_t = 6$ s) and subsampling the result. (*B*) The phase in radians of the best-correlated harmonic at the stimulus alternation frequency (1/32 Hz) is shown as a function of position along the region of interest. (*C*) An anatomical image in the plane of the calcarine is shown. The black line shows the gray matter along the calcarine that was used for the region of interest. The data are from subject BW.

because its fundus, which is closer to the lateral aspect of the brain, appears as a dark band, and its lips appear as light regions surrounding the sulcus. [In subsequent figures we use color or brightness to represent functional data. On these flattened representations, we will continue to indicate the positions of the deepest part of the calcarine sulcus (dashed line) and the occipital pole (star).]

We evaluated how accurately the algorithm preserved distances between gray matter points by comparing, for each pair of points, the separation in the cortical manifold and in the flattened representation. For the points shown in the figure, spanning over a 100 cm^2 region of gray matter, distances between pairs of points in the image of flattened cortex differed from the true cortical manifold distances with a roughly Gaussian distribution with an SD of 3 mm.

Results

Basic Measurements

The first set of experiments showed that the moving ring stimulus created a traveling wave of activity that could be observed in the fMRI signal. We used a contracting ring stimulus, measured the fMRI signal in a plane parallel to the calcarine sulcus and analyzed data along the linear region of interest within area V1 indicated in black in Figure 4*C*. We expected the stimulus to create a traveling wave of activity moving from anterior to posterior along the region of interest.

Figure 4*A* shows the time varying fMRI signal at points along the region of interest. The fMRI signal is a traveling wave that moves from anterior to posterior portions of cortex. Figure 4*B* shows the delay in activity at points along the region of interest, as measured by the response phase. This plot shows that, as expected, the fMRI signal was delayed at posterior portions of the calcarine relative to the signal at more anterior locations.

Figure 5 shows the results of a similar traveling wave experiment displayed on a flattened image of cortex. In these five images the gray level values reflect the spatial pattern of the fMRI response magnitude at different moments in time during the stimulus cycle. The fMRI signal shown in Figure 5 was generated during an experiment in which the stimulus consisted of contracting ring stimuli with one ring. The stimulus alternation frequency was 1/32 Hz. In Figure 5 each pixel's gray level represents the response magnitude multiplied by a unit harmonic at the response phase. These images represent that portion of the fMRI signal at the stimulus frequency. The bright band of fMRI signal in the images shifts along the cortex. (A more finely sampled sequence of these images as a movie can be seen at http://white.stanford.edu/wandell)

We have measured this traveling wave in many experiments on 12 subjects. While the signal-to-noise varied among subjects, most locations where the scan plane intersected the posterior calcarine sulcus yielded a signal that easily stood out from noise. The traveling wave has also been measured by other

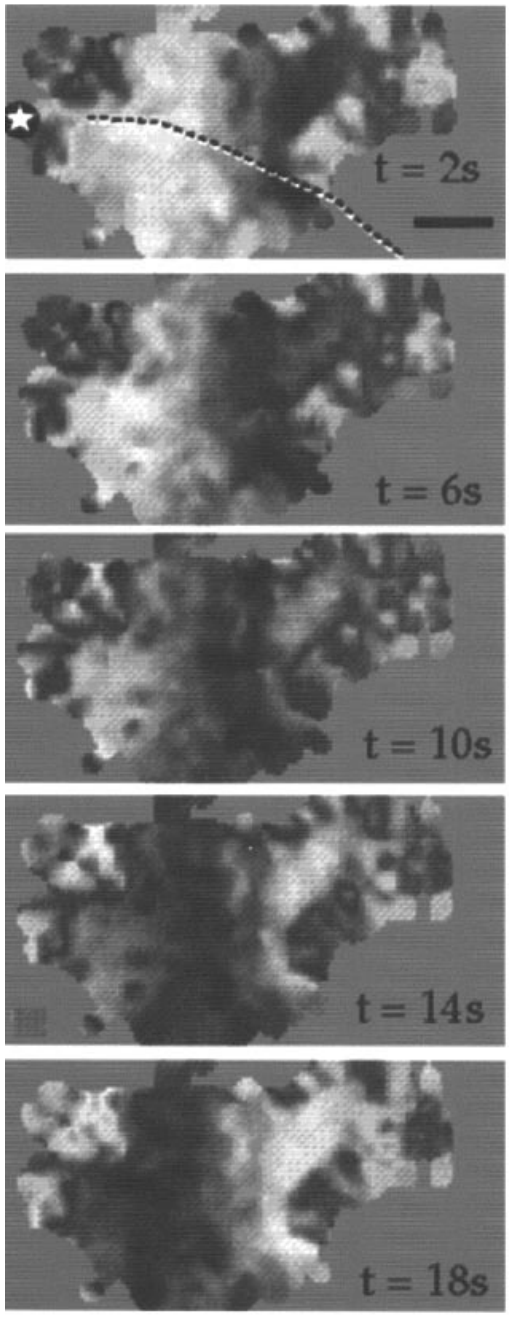

Figure 5. The traveling wave of fMRI response at different moments in time is shown on a flattened representation of cortex. The stimulus was a single contracting ring. The five images show the activity estimated at times separated by one-eighth of the stimulus alternation period (32 s). The brightness represents response magnitude at the stimulus frequency as described in the text. The dashed line traces the deepest part of the calcarine sulcus; the star indicates the occipital pole. Data are from subject BW.

investigators (DeYoe *et al.*, 1994, 1996; Sereno *et al.*, 1995). Here, we report mainly on the data measured from the brains of the two authors.

Luminance Defined Rings

We used a modified moving ring stimulus to confirm that the traveling wave response is caused by stimulus contrast rather than by stimulus luminance differences. The modified moving rings were white and spatially uniform. The luminance of the ring was 184 cd/m^2 and they were presented on a uniform gray field with 92 cd/m^2 luminance. The temporal period of the rings was 1/48 Hz, and four cycles were shown. In a second experiment, subjects saw rings composed of contrast-reversing checkerboard; other parameters were the same as for the luminance rings.

Average responses to the two types of stimuli are compared in Figure 6. The contrast-reversing checkerboard generated a sustained response; the luminance ring generated a transient response at the borders of the ring (Fig. 6*A*). Because each ring has two borders, the temporal frequency of the response to the luminance rings was twice that of the response to the checkerboard rings (Fig. 6*B*). These measurements show that activity in area V1 is caused mainly by local contrast.

Retinotopy

Polar Angle

There are several retinotopically organized areas near V1. In the macaque and owl monkey, area V1 is surrounded by area V2 (Zeki, 1969; Allman and Kaas, 1974). As one moves from the middle of V1 to the V1/V2 border, the receptive field locations change from the horizontal to the vertical meridian. As one crosses the border from V1 and continues into V2, the receptive field locations move from the vertical meridian back towards the horizontal meridian; there is a reversal in the direction of change of retinotopy with respect to polar angle at the V1/V2 border. This reversal occurs at the upper vertical meridian ventrally and at the lower vertical meridian dorsally. Additional work on monkeys suggests that similar reversals would occur at the V2/V3 and V2/VP borders (Zeki, 1969; Van Essen and Zeki, 1978, Gattass *et al.*, 1988). Figure 1*B* illustrates a proposed analogous organization for human cortex (Horton and Hoyt, 1991b).

In short, boundaries of early retinotopically organized visual areas are defined by reversals in the representation of the polar angle. Hence, measurements made with the rotating wedge stimulus are well-suited for delimiting these boundaries. In an experiment designed to identify these early visual areas, three subjects viewed a rotating wedge stimulus at a frequency of 1/48 Hz and a flicker rate of 8 Hz.

Figure 7 shows the polar angle calculated from the response phase of the fMRI signal. Data from three subjects are shown in the three panels. To compute the polar angle from the phase of the measured fMRI signal, we located the clear reversals in the response phase located on the upper and lower lips of the calcarine sulcus and assumed that these locations represented the lower and upper vertical meridia. The reversals corresponding to the V1/V2 borders are clearly visible. Another reversal is evident on the dorsal surface, presumably corresponding to V2/V3. Notice that the dorsal half of V2 represents only a quarter of the visual field, as expected. Finally, the ventral V2/VP boundary can also be observed in some cases. We have observed similar results in several additional subjects; our data are in substantial agreement with measurements from other laboratories (Schneider *et al.*, 1993; Sereno *et al.*, 1995; Shipp *et al.*, 1995; Tootell *et al.*, 1995; DeYoe *et al.*, 1996).

Eccentricity

Retinotopy with respect to eccentricity was measured using a contracting ring stimulus with a frequency of 1/32 Hz. We inferred eccentricity from the response phases by calculating the

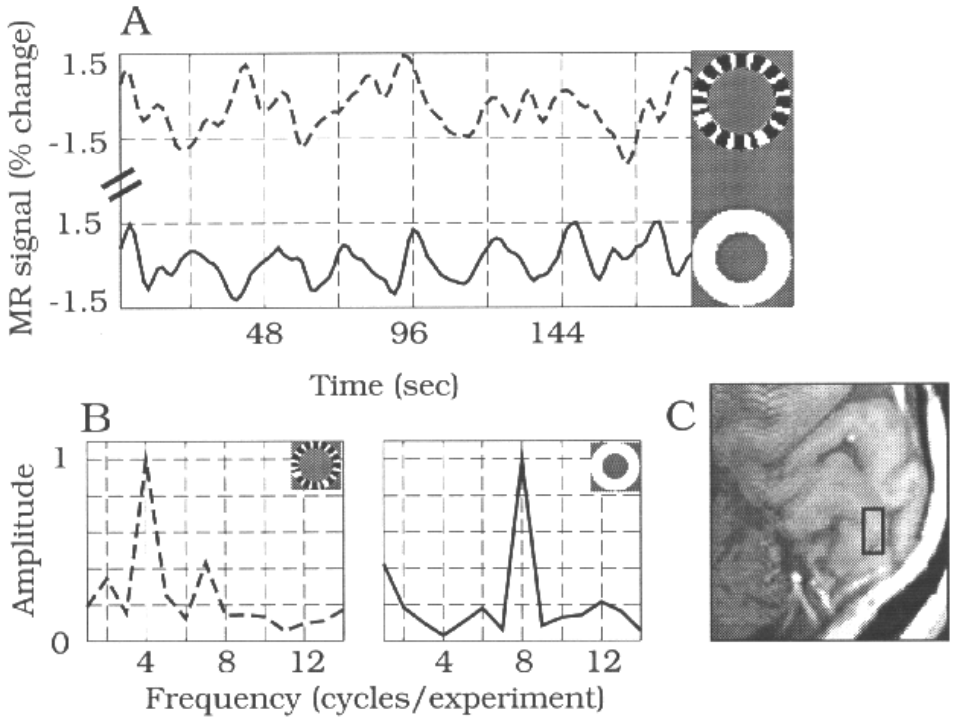

Figure 6. Comparison of responses to checkerboard rings and luminance rings. (*A*) Average responses to four periods of an expanding ring stimulus defined by a contrast-reversing checkerboard (dashed line) and a luminance step (solid line) are shown. The contrast-reversing checkerboard generated a sustained response; the luminance ring generated a transient response at the borders of the ring. The time series were smoothed by convolution with a Gaussian ($\sigma_t = 6$ s) for display purposes. (*B*) The normalized average amplitude spectra of pixel time series in the region of interest are shown. The spectrum created by the checkerboard stimulus peaks at four cycles per experiment, while the spectrum created by the luminance ring peaks at eight cycles. These spectra were computed without the Gaussian convolution. (*C*) The fMRI time series were averaged within the region of interest shown by the box. The data are from subject BW.

expected phase of activation for each stimulus eccentricity given a simple linear model of the cortical hemodynamics. The model represents the hemodynamics by a temporal impulse response function. We predicted the temporal delay in the fMRI signal by convolving the stimulus timecourse at each visual eccentricity (see Fig. 2*B*) with the model impulse response. The model impulse response was derived by Boynton *et al.* (1996) and resembles models proposed by others (Friston *et al.*, 1994; Lange and Zeger, 1996).

Figure 8 shows a flattened representation of the cortical sheet. The color at each point represents the visual eccentricity encoded at that position. The foveal response is visible in posterior cortex. Increasingly anterior locations respond to increasingly eccentric stimuli. Retinotopically organized responses extend along a 3–4 cm strip of cortex. Beyond this region (indicated by the black line in the figure) the responses resemble noise, presumably because this part of cortex represents visual field eccentricities beyond the 12° stimulus radius. A similar noisy region is present near the occipital pole. The region of cortex represented in this image is smaller than those shown in Figure 7 because we used scan planes parallel to the calcarine sulcus to map eccentricity. These scan planes intersected less extrastriate cortex than the perpendicular scan planes used to map the polar angle.

To compare these results with other measurements of human V1 retinotopy we plotted average eccentricity as a function of cortical distance. We measured the cortical distance from each pixel to a line close to the posterior border of V1. This line was selected by hand using maps of activity such as the one in Figure 8. We drew the line parallel to the iso-eccentricity bands evident in the map, and at the most posterior section of the map that contained reliable responses. Distances to the line from each point in gray matter were computed using a flood-fill algorithm. The algorithm found the shortest three-dimensional path between points in the volume of gray matter. Cortical distances were grouped into bins and the average eccentricity within each bin was computed.

Figure 9 shows the results of this analysis for four hemi-

Figure 7. Retinotopy with respect to polar angle measured using the rotating wedge stimulus is shown. Color codes the polar angle as indicated on the upper right: UVM is the upper vertical meridian, HM is the horizontal meridian and LVM is the lower vertical meridian. Reversals in the change of the polar angle representation can be identified at positions above and below the calcarine sulcus. The locations identify the boundary between areas V1 and V2. The other reversals identify the V2/V3 boundary and the V2/VP boundary. The dashed line traces the deepest part of the calcarine sulcus; the star indicates the position of the occipital pole. Data are from three different subjects.

Figure 8. Retinotopy with respect to eccentricity on a flattened representation of cortex is shown. The color of each pixel represents the visual eccentricity encoded at that position. The correspondence between eccentricity and color is shown on the upper right; the stimulus covered eccentricities from 2 to 12°. Visual eccentricity was computed from response phase as described in the text. The dashed line traces the deepest part of the calcarine sulcus; the star indicates the position of the occipital pole. Data beyond the solid black line are uncorrelated with the stimulus and represent portions of the visual field beyond our display. Data are from subject SE.

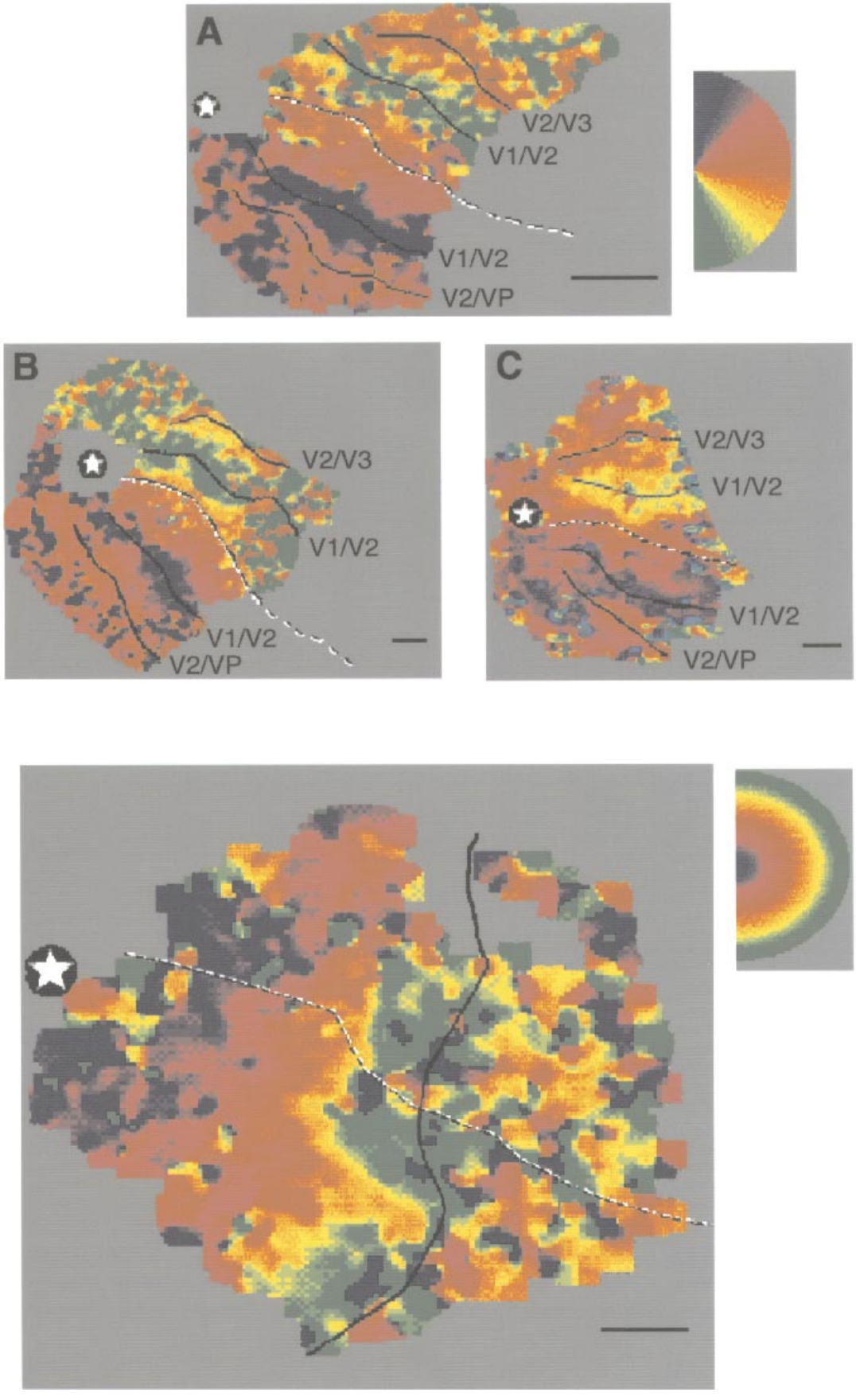
A
V2/V3
V1/V2
V1/V2
V2/VP
B
V2/V3
V1/V2
V1/V2
V2/VP
C
V2/V3
V1/V2
V1/V2
V2/VP

spheres. The line that was used to measure cortical distance fell at positions that represented slightly different eccentricities in the different hemispheres. To compare data across hemispheres, we aligned the four data sets at the point representing 10° of eccentricity. The smooth curve is the exponential function exp(0.063(d + 36.54)) that best fit (least-squares) the data, where d is the cortical distance in mm.

Spatial Localization

Next, we measured how accurately the response to the moving ring stimulus can be localized. The measurements were based on the following logic. Consider the response to a single frame of the moving ring stimulus. The cortical locations responding to that frame are those locations whose fMRI signal has a particular response phase. Cortical locations responding to the next frame in the stimulus will have a slightly different response phase. Thus, the response to a particular stimulus frame will be well localized when the cortical locations with its response phase can be reliably discriminated from the cortical locations at the response phase of the next frame. Factors such as noise in the fMRI signal and spatial and temporal sampling limit our ability to localize the response phase.

To measure how accurately the response phases can be localized, we made measurements in a plane within the calcarine sulcus. The measurement plane intersected linear regions in both the right and the left calcarine sulci. The stimulus contained two contrast-reversing rings. In one experiment the rings traveled outward (expanding) and in a second experiment they traveled toward the fixation mark (contracting). The stimulus period was 48 s and the experiment lasted for four periods.

In order to calculate the localization precision we estimated the response phase separately for each stimulus cycle and each pixel. These estimates were used to compute a mean and standard error of the phase for each pixel. Figure 10 shows the mean and standard errors of the phase estimated within two regions of interest for the two stimuli.

The modal standard error of the phase estimate across pixels in both regions of interest was 0.33 radians. The modal values were similar in the right and left calcarine, and for expanding and contracting rings. The modal rate of change of the temporal phase along the two regions of interest (i.e. the slopes of the lines in Figure 10) was ~0.60 radians/mm. Hence, a reliable (two standard errors of the mean) phase separation corresponds to 0.66 rad/0.60 (rad/mm) 1.1 mm, which is close to our previous estimate of 1.3 mm (Engel *et al.*, 1994).

We interpret this value as an upper bound on the precision of the localization under these conditions. Of course, differences in stimuli, brain regions and signal-to-noise ratios will influence the spatial localization obtainable in other conditions.

Spatial Resolution

We evaluated the spatial resolution of the fMRI signal by estimating the modulation transfer function (MTF). In general, the MTF describes how the signal varies with increasing spatial frequency. We used the MTF to analyze how well the fMRI signal captures the spatial pattern of cortical activity.

To generate patterns of cortical activity at increasing spatial frequency, we used stimuli with one, two, three and four moving rings. The temporal frequency of the stimuli in all four conditions moved was held constant at 1/48 Hz by adjusting the velocity of the moving rings. The rings reversed their contrast at 8 Hz.

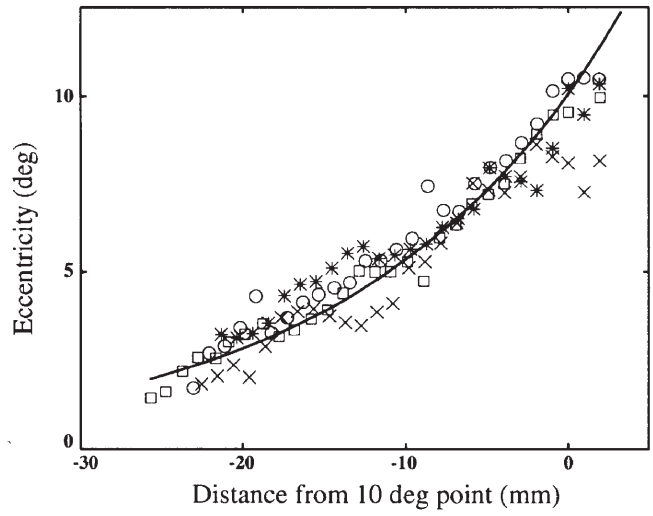

Figure 9. Visual field eccentricity as a function of distance from the 10° point in V1 is shown for four hemispheres. Eccentricity was computed from response phase; cortical distances were measured along the gray matter from a line close to the posterior border of V1. Cortical distances were grouped into bins and the average eccentricity within each bin was computed. Each symbol type represents data from one hemisphere from either subject SE or BW. The data have been shifted to align at the 10° eccentricity point. The smooth curve is the exponential function exp(0.063(d + 36.54)) that best fit (least-squares) the data, where d is cortical distance (mm).

We expected each ring to generate a traveling wave of activity. As the number of stimulus rings increased, the distance between the traveling waves decreased and the falling edge of one wave overlapped with the rising edge of its neighboring wave. Increasing the stimulus spatial frequency caused more overlap and reduced the temporal modulation of the fMRI signal measured at each pixel. Thus, we evaluated spatial resolution by measuring the fall off in the response magnitude as a function of the cortical separation between the traveling waves. We measured the separation between the waves in terms of their cortical frequency, which has units of cycles per mm of cortex.

Cortical frequency at each location in gray matter was calculated using measurements of retinotopy with respect to eccentricity. As described earlier, these measurements can be summarized by computing an exponential function that relates eccentricity to cortical distance (see Fig. 9 and accompanying text). We estimated the parameters of one such function for each hemisphere using the data obtained in the one ring condition. The derivative of this function specified the the number of degrees of visual angle represented in 1 mm of cortex at each gray matter location (deg/mm) for that hemisphere. Multiplying the stimulus spatial frequency (cycles/deg) by this derivative (deg/mm) yielded the cortical frequency (cycles/mm) for each gray matter location.

We estimated the MTF by plotting response magnitudes from all four stimulus conditions and gray matter locations as a function of cortical frequency. Figure 11 shows such a plot for one hemisphere. To make this plot, data were binned by cortical frequency and the average of each bin is plotted. The smooth curve is a scaled Gaussian (SD = 0.11 cycles/mm) fit to these averages (least-squares) after subtracting out a baseline correlation that represents correlation due to noise. (The baseline correlation was estimated in two ways. We measured correlations in peripheral regions of V1 that showed no coherent

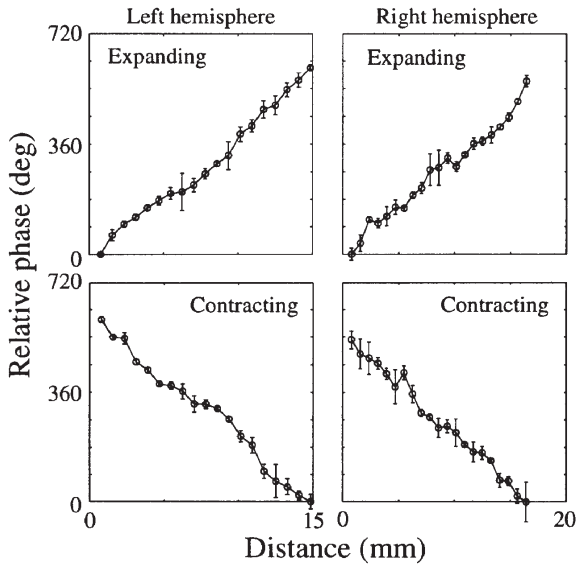

Figure 10. Standard errors of the response phase measurements were used to estimate localization precision. Response phases were estimated separately for each stimulus cycle. The mean and standard error of the estimates at various positions along the calcarine sulcus are shown. Error bars represent 2 standard errors. The top panels show measurements using expanding rings and the bottom panels show measurements with contracting rings. Panels on the left show measurements from the left calcarine and panels on the right from the right calcarine. The data are from subject BW.

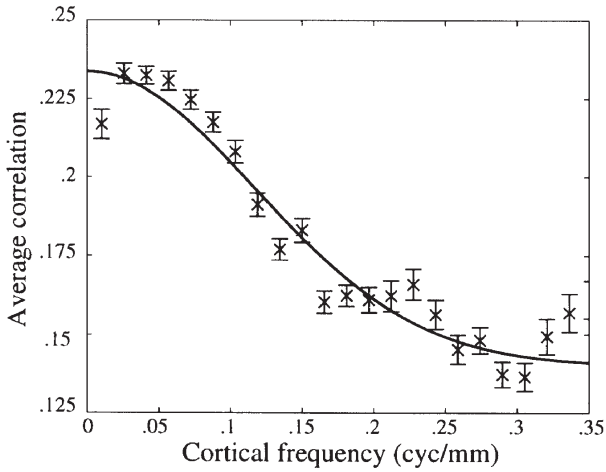

Figure 11. Analysis of the spatial resolution of fMRI. Average fMRI response magnitude is shown as a function of cortical frequency. Cortical frequency was calculated as described in the text. The error bars represent 2 standard errors. The smooth curve is the scaled Gaussian (SD = 0.11) that best fits (least-squares) the data. The Gaussian function falls to 60.65% of its maximum at 1 SD from the mean; so, the average correlation is at roughly sixty percent of its maximum at 0.11 cycles/mm, or 1 cycle per 9 mm. These data are from subject BW.

signal. We also examined correlations to harmonics that differed from the stimulus frequency. The two estimates agreed well.)

We performed this experiment in two subjects (four hemispheres) and the estimated SDs were 0.19, 0.11, 0.08, 0.07, yielding a mean of 0.11. The Gaussian function falls to 60.65% of its maximum at 1 SD from the mean. On average, then, the signal amplitude falls to ~60% of its maximum at 0.11 cycles/mm or equivalently at 1 cycle in 9 mm of cortex.

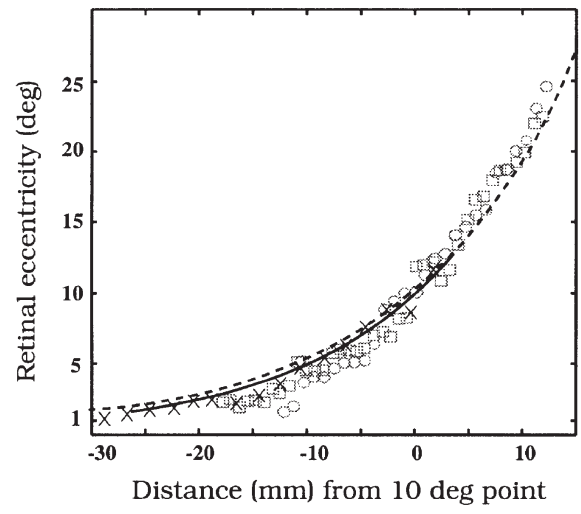

Figure 12. Comparison of retinotopic measurements of human V1. Retinal eccentricity as a function of cortical distance relative to the 10° point is shown. The open symbols are measurements from two observers in Engel *et al*. (1994). The solid curve shows the best fitting exponential (least-squares) to the four hemispheres measured in this study. The dotted line shows an estimate derived from scotoma in human stroke patients and electrophysiological data from non-human primates (Horton and Hoyt, 1991a). The 'x's are fMRI measurements by Sereno *et al.* (1995).

Discussion

Visual Areas

One of the most important applications of the traveling wave measurements is the segregation of retinotopically organized visual areas in human cortex. Our method segregates these visual areas clearly and reliably, and this observation has been confirmed by other groups (e.g. Sereno *et al.*, 1995; DeYoe *et al.*, 1996). We have measured both borders of a retinotopically organized region surrounding V1, revealing a likely candidate for human V2. Retinotopic organization continues beyond this region to presumptive V2/V3 and V2/VP borders as well. Figure 7 shows three good examples of these borders. These results also agree with measurements made using static stimuli (Schneider *et al.*, 1993; Shipp *et al.*, 1995; Tootell *et al.*, 1995).

V1 Retinotopy

Figure 12 shows our results along with other estimates of the retinotopic organization of human primary visual cortex. The solid black line is an exponential curve fit to the data shown in Figure 9. The open symbols were computed from two linear regions of interest in single plane expanding ring experiments (Engel *et al.*, 1994). The dashed line is an estimate based on human stroke patients and electrophysiological data from non-human primates (Horton and Hoyt, 1991a); the 'x's are from Sereno *et al.* (1995), who used fMRI methods similar to the ones described here. To compare the various results, we aligned the data at the location of the representation of the 10° point. There is substantial agreement among all these measurements as well as those obtained using other methods (see figure 2 in Engel *et al.*, 1994).

There have been two different reports concerning the extent of the representation of the central 2° in the human area V1. Horton and Hoyt (1991a) report that the central 2° covers <20 mm of cortical distance; Sereno *et al.* (1995) suggest that the central 2° extends over >30 mm of cortical distance. Because the

fixation spot in our experiments occupied the central 0.5°, and because of the presence of small eye movements, we could not make measurements below 1°. However, in our data the representation of the 2° point generally falls in a part of V1 found near the posterior pole. Our measurements could be consistent with those of Sereno *et al.* (1995) if area V1 extends at least 3 cm around the posterior pole onto the lateral surface. While anatomical investigations agree that V1 can extend onto the lateral surface, none finds such a large extension (Stensaas *et al.*, 1974; Rademacher *et al.*, 1993). Hence, our measurements are in general agreement with those of Horton and Hoyt (1991a).

Localization and Resolution

Our measurements of the traveling wave show that the fMRI signal can be localized to within 1.1 mm. This precision was achieved in 192 s experiments using a 1.5T instrument. Our measurements of response magnitude as a function of cortical frequency of the traveling wave show that the modulation transfer function falls off as a Gaussian function with an SD of 0.11 cycles/mm. Signals at higher cortical frequencies can be measured; the upper limit on detectable cortical frequency depends on the signal-to-noise ratio of the measurement.

To the extent that the relationship between neural activity and the fMRI signal can be modeled accurately by a symmetric shift-invariant linear system, the system's linespread function can be computed directly from its MTF (e.g. Bracewell, 1978). Intuitively, the linespread function defines the cortical spread measured when stimulating with a very fine flickering line, and when the MTF is a Gaussian function, the linespread is also Gaussian. We have not tested whether the relationship between neural activity and the fMRI signal is linear; should this test fail, neither the linespread nor the MTF completely characterize the spatial resolution of the fMRI signal. We computed that the linespread function associated with our MTF measurements is a Gaussian function with a full width at half maximum amplitude of 3.5 mm. This value is close to the neural linespread estimated in the macaque by optical imaging with voltage sensitive dye (Grinvald *et al.*, 1994).

There are several potential sources of the spatial spread in the fMRI signal. A portion of the spread may be due to lateral neural connections within the cortex; another portion may be due to the response of the vasculature to focal neural activity; finally, some part of the spreading must be due to experimental artifacts such as slight head movements, brain pulsatility and optical defocus. The agreement between the fMRI measurements and the neural linespread estimated in the macaque (Grinvald *et al.*, 1994) suggests that lateral connections in V1 may be the limiting factor in the spatial resolution of the fMRI signal.

For a number of reasons the localization and resolution estimates obtained in these experiments may not provide a general rule for the brain. First, the vascularization in area V1 is relatively dense (Zheng *et al.*, 1991). Both localization and resolution precision may depend upon this vascularization. Second, localization and resolution depend on the signal-to-noise ratio, which depends on a number of factors, including the stimulus, task, brain region, pulse sequence and MR device. Third, for many parts of the brain we do not yet know how to create stimuli or tasks that generate focal activity. Consequently, it is not possible to generalize from the measurements reported here to experiments in other brain regions. Nonetheless, our results do show quite clearly that fMRI can yield fine spatial precision in experiments lasting only a few minutes.

Source of the fMRI Signal

Because BOLD contrast arises from changes in blood oxygenation, large veins produce measurable signal. Some research suggests that most of the signal comes from macroscopic vessels (Lai *et al.*, 1993). This would present a problem for some fMRI applications because large vessels pool blood from relatively large regions of cortex and their oxygenation level only informs us about the average activity over these regions. Whether the BOLD contrast arises only from large veins is controversial; some evidence suggests that a significant portion of the signal arises from the cortical capillary bed (Menon *et al.*, 1995).

Our estimate of the MTF supports the view that a significant portion of the fMRI signal arises from vessels serving fairly small regions of cortex. Figure 11 shows that we observe significant correlations at cortical frequencies at least as high as 1 cycle per 6 mm (0.1667 cycles/mm). Hence, vessels serving significantly less than 6 mm of cortex must contribute to the fMRI signal.

The methods and results in this paper demonstrate several imporant aspects of our ability to measure the activity in human visual cortex. First, we can identify the locations of several different retinotopically organized areas near V1 reliably and efficiently. Second, measurements of the fMRI signal in these areas reflect neural activity within a small patch of cortex. Third, the fMRI signal is strong enough to measure reliable stimulus response functions, such as the signal dependence on visual field location, contrast, color or other properties of the visual stimulus.

Taken together, these advances imply that fMRI studies can move beyond cortical localization experiments; that is, beyond experimental protocols that seek to measure only where activity is present. Instead, fMRI measurements can be used to characterize the computational properties of neural populations within functionally and anatomically meaningful visual areas. These measurements can be structured to be analogous to electrophysiological measurements of individual neurons' receptive fields. Preliminary results from this new style of imaging experiment have already appeared, including parameteric studies of neural population response to contrast (Tootell *et al.*, 1995; Boynton, *et al.*, 1996), color (Engel and Wandell 1996) and spatial pattern (Demb *et al.*, 1996). Examining how these population responses vary across visual areas will help to specify the sequence of neural transformations underlying visual perception.

Appendix: Calculating Response Phase and Response Magnitude

Many analyses of fMRI data are based on the method of correlating pixel time series with a fixed function that serves as a probe for measuring response properties (Bandettini *et al.*, 1993). In this appendix we give informal proofs of two facts concerning the correlation of time series data with a harmonic probe function at frequency F. First, we show that the correlation is maximized when the phase of the harmonic equals the phase of the time series' Fourier component at frequency F. Second, we show that the maximum correlation value of the harmonic with the time series data is the amplitude of the time series Fourier component at fiequency F divided by the square root of the time series power.

First, we recall that the definition of the correlation of two column vectors with zero mean, u and v is

$$c(u,v) = \frac{u^t v}{\|u\|\|v\|} \quad (1)$$

To simplify the analysis we remove the mean from the time series data at each pixel. We use d as a column vector of length N to represent the time series data at a pixel. We denote the sampled harmonic function at frequency f and phase ϕ by the vector $h(f, \phi) = \sin((2\pi ft/N) + \phi)$, where $t = 1,..,N$ represents the temporal samples. Finally, suppose the stimulus frequency is F.

We can express the correlation between the data and a probe harmonic at the stimulus frequency using equation (1)

$$c\left(h(F,\Phi),d\right) = \frac{h(F,\Phi)^t d}{\|h(F,\Phi)\|\|d\|} \quad (2)$$

Next, we express the time series data in terms of its discrete Fourier series (DFS),

$$d = \sum_{f=0}^{N-1} a_f \sin\left(\frac{2\pi ft}{N} + \phi_f\right) \quad (3)$$

where a_f and ϕ_f are the amplitude and phase of the harmonic component at frequency f. Substituting equation (3) into equation (2) yields

$$c\left(h(F,\Phi),d\right) = \frac{h(F,\Phi)^t\left(\sum_{f=0}^{N-1} a_f h\left(F,\phi_f\right)\right)}{\sqrt{\frac{N}{2}}\left\|\sum_{f=0}^{N-1} a_f h\left(f,\phi_f\right)\right\|} \quad (4)$$

Because the harmonics form an orthogonal basis the dot products between harmonics with unequal frequencies are zero. This simplifies equation (4) to

$$c\left(h(F,\Phi),d\right) = \frac{h(F,\Phi)^t\left(a_F h\left(F,\phi_f\right)\right)}{\sqrt{\frac{N}{2}}\sqrt{\sum_{f=0}^{N-1}\left(a_f h\left(f,\phi_f\right)\right)\left(a_f h\left(f,\phi_f\right)\right)}} \quad (5)$$

which further reduces to

$$c\left(h(F,\Phi),d\right) = \frac{h(F,\Phi)^t\left(a_F h\left(F,\phi_f\right)\right)}{\frac{N}{2}\sqrt{\sum_{f=0}^{N-1} a_f^2}} \quad (6)$$

It follows from equation (6) that the correlation between the harmonic at the stimulus frequency and the time series data is maximized when $h(F, \Phi)^t(a_F h(F, \phi_f))$ is maximized. This dot product is greatest when the phase of the probe harmonic and the corresponding Fourier series component are the same, $\phi_f = \Phi$ (e.g. Bracewell 1978). Hence, the correlation is also maximized when the two phases are equal.

Now consider the value of the maximum correlation. First, set $\Phi = \phi_f$ in equation (6) because this maximizes the correlation. Next, because $h(F, \phi_f)^t h(F, \phi_f) = \sqrt{(N/2)}$ for $f > 0$, we can simplify equation (6) to

$$c\left(h(F,\phi_f),d\right) = \frac{a_F}{\sqrt{\sum_{f=0}^{N-1} a_f^2}} \quad (7)$$

Equation (7) demonstrates that the maximum correlation value of the harmonic with the time series data is the amplitude of the time series' Fourier component at frequency F divided by the square root of the time series power.

Notes

We thank Heidi Baseler, Geoffrey Boynton, Eduardo-Jose Chichilnisky, Jonathan Demb, David Heeger, William Newsome, Phillip Servos, Michael Shadlen and David Tolhurst for their discussions and comments on the manuscript. We also thank two anonymous reviewers for their comments. This work was supported in part by the McDonnell-Pew Foundation, the Hewlett-Packard Corporation, the R. S. Lucas Center, and NEI grants ROI EY03164 and P41 RR09784.

Address correspondence to Stephen Engel, UCLA Psychology Department, Franz Hall 1285 Los Angeles, CA 90095-1563, USA.

References

Allman JM, Kaas JH (1974) The organization of the second visual area (V ii) in the owl monkey: a second order transformation of the visual hemifield. Brain Res 76:247–265.

Arun KS, TS Huang, SD Blotstein (1987) Least-squares fitting of two 3-d point sets. IEEE PAMI 9:698–700.

Bandettini PA, Jesmanowicz A, Wong EC, Hyde JS (1993) Processing strategies for time-course data sets in functional MRI of the human brain. Magn Reson Med 30:161–173.

Boynton GM, Engel SA, Glover GH, Heeger DH (1996) Linear systems analysis of fMRI in human v1. J Neurosci 16:4207–4221,

Bracewell R (1978) The Fourier transform and its applications. New York: McGraw-Hill.

Carman GJ, Drury HA, Van Essen DC (1995) Computational methods for reconstructing and unfolding the cerebral cortex. Cereb Cortex 5:506–517.

Dale AM, Sereno MI (1993) Improved localization of cortical activity by combining EEG and MEG with MRI cortical surface reconstruction: a linear approach. J Cogn Neurosci 5:162–176.

Demb JB, Boynton GM, Heeger DJ (1996) Evidence for neural suppression in human visual cortex. Neuroimage 3:S269.

DeYoe EA, Bandettini P, Neitz J, Miller D, Winans P (1994) Functional magnetic resonance imaging (fMRI) of the human brain. J Neurosci Methods 54:171–187.

DeYoe EA, Carman GJ, Bandettini P, Glickman S, Wieser J, Cox R, Miller D, Neitz J (1996) Mapping striate and extrastriate visual areas in human cerebral cortex. Proc Natl Acad Sci USA 93:2382–2386.

Drury HA, Van Essen DC, Anderson CH, Lee CW, Coogan TA, Lewis JW (1996) Computerized mappings of the cerebral cortex: a multi-resolution flattening method and a surface-based coordinate system. J Cogn Neurosci 8:1–28.

Engel SA, Wandell BA (1996) Color opponent processing in human visual cortex measured with functional MRI. Soc Neurosci Abstr 21:18.

Engel SA, Rumelhart DE, Wandell BA, Lee AT, Glover GH, Chichilnisky EJ, Shadlen MN, Newsome WT (1993) Functional MRI measurements of human striate cortex topography. Soc Neurosci Abstr 19:335.

Engel SA, Rumelhart DE, Wandell BA, Lee AT, Glover GH, Chichilnisky EJ, Shadlen MN(1994) fmri of human visual cortex. Nature 369:525.

Fox PT, Miezin F, Allman J, Van Essen DC, Raichle ME (1987) Retinotopic organization of human visual cortex mapped with positron-emission tomography. J Neurosci 7:913–922.

Friston KJ, Jezzard P, Turner R (1994) Analysis of functional MRI time-series. Hum Brain Map 1:153–171.

Gattass R, Sousa APB, Gross CG (1988) Visiotopic organization and extent of V3 and V4 of the macaque. J Neurosci 8:1831–1845.

Grinvald A, Lieke EE, Frostig RD, Hildesheim R (1994) Cortical point-spread function and long-range lateral interactions revealed by real-time optical imaging of macaque monkey primary visual cortex. J Neurosci 14:2545–2568.

Holmes G (1918) Disturbances of vision by cerebral lesions. Br J Ophthal 2:353–384.

Holmes G (1944) The organization of the visual cortex in man. Proc Roy Soc B, 132:348–361.

Horton J, Hoyt W (1991a) The representation of the visual field in human striate cortex. Arch Ophthalmol 109:816–824.

Horton JC, Hoyt WF (1991b) Quadrantic visual field defects: a hallmark of lesions in extrastriate (V2/V3) cortex. Brain 114:1703–1718.

Kwong KK, Belliveau JW, Chesler DA, Goldberg IE, Weisskoff RM, Poncelet BP, Kennedy DN, Hoppel BE, Cohen MS, Turner R, Cheng H, Brady TJ, Rosen BR (1992) Dynamic magnetic resonance imaging of human brain activity during primary sensory stimulation. Proc Natl Acad Sci USA 89:5675–5679.

Lai S, Hopkins AL, Haacke EM, Li D, Wasserman BA, Buckley P, Friedman L, Metzler H, Hedera P, Fiedland R (1993) Identification of vascular structures as a major source of signal contrast in high resolution 2d and 3d functional activation imaging of the motor cortex at 15t: preliminary results. Magn Reson Med 30:387–392.

Lange N, Zeger SL (1996) Non-linear Fourier analysis of magnetic resonance functional neuroimage time series. J Roy Statist Soc B (in press).

Menon RS, Ogawa S, Hu X, Strupp JP, Anderson P, Ugurbil K (1995) BOLD based functional MRI at 4 tesla includes a capillary bed contribution: echo-planar imaging correlates with previous optical imaging using intrinsic signals. Magn Reson Med 33:453–459.

Meyer CH, Hsu BS, Nishimura DG, Macovski A (1992) Fast spiral coronary artery imaging. Magn Reson Med 28:202–213.

Ogawa S, Tank D, Menon R, Ellermann J, Kim S, Merkle H, Ugurbil K (1992) Intrinsic signal changes accompanying sensory stimulation: functional brain mapping with magnetic resonance imaging. Proc Natl Acad Sci USA 89:591–5955.

Rademacher J, Caviness VS, Steinmetz H, Galaburda AM (1993) Topographic variation of the human primary cortices: implications for neuroimaging, brain mapping, neurobiology. Cereb Cortex 3:313–329.

Schneider W, Noll DC, Cohen JD (1993) Functional topographic mapping of the cortical ribbon in human vision with magnetic resonance imaging. Nature 365:150–153.

Schwartz EL (1990) Computer aided neuroanatomy of macaque visual cortex. In: Computational neuroscience (Schwartz EL ed), pp 295–315. Cambridge, MA: MIT Press.

Sereno MI, Dale AM, Reppas JB, Kwong KK, Belliveau JW, Brady TJ, Rosen BR, Tootell RB (1995) Borders of multiple human visual areas in humans revealed by functional MRI. Science 268:889–893.

Shipp S, Watson JDG, Frackowiak RSJ, Zeki S (1995) Retinotopic maps in human prestriate visual cortex: the demarcation of areas v2 and v3. Neuroimage 2:125–132.

Stensaas SS, Eddington DK, Dobelle WH (1974) The topography and variability of the primary visual cortex in man. J Neurosurg 40:747–755.

Tootell RGH, Reppas JB, Kwong KK, Malach R, Born RT, Brady TJ, Rosen BR, Belliveau JW (1995) Functional analysis of human MT and related visual cortical areas using magnetic resonance imaging. J Neurosci 15:3215–3230.

Van Essen DC, Zeki SM (1978) The topographic organization of rhesus monkey prestriate cortex. J Physiol 277:193–226.

Wandell BA, Engel SA, Hel-Or HZ (1996) Creating images of the flattened cortical sheet. Invest Ophthalmol Vis Sci 37:S1081.

Worden M, Schneider W, Wellington R (1995) Assessing the distribution of exogenous and endogenous attentional modulation in human visual cortex with fMRI. Program of the Annual Meeting of the Psychonomic Society 36:28.

Zeki SM (1969) Representation of central visual fields in prestriate cortex of monkey. Brain Res 14:271–291.

Zheng D, LaMantia AS, Purves D (1991) Specialized vascularization of the primate visual cortex. J Neurosci 11:2622–2629.